Nonlinear laser lithography for indefinitely large-area nanostructuring with femtosecond pulses

Bülent Öktem[1†], Ihor Pavlov[2,3†], Serim Ilday[4], Hamit Kalaycıoğlu[2], Andrey Rybak[2,3], Seydi Yavaş[1], Mutlu Erdoğan[1] and F. Ömer Ilday[2]*

Dynamical systems based on the interplay of nonlinear feedback mechanisms are ubiquitous in nature[1-5]. Well-understood examples from photonics include mode locking[6] and a broad class of fractal optics[7], including self-similarity[8]. In addition to the fundamental interest in such systems, fascinating technical functionalities that are difficult or even impossible to achieve with linear systems can emerge naturally from them[7] if the right control tools can be applied. Here, we demonstrate a method that exploits positive nonlocal feedback to initiate, and negative local feedback to regulate, the growth of ultrafast laser-induced metal–oxide nanostructures with unprecedented uniformity, at high speed, low cost and on non-planar or flexible surfaces. The nonlocal nature of the feedback allows us to stitch the nanostructures seamlessly, enabling coverage of indefinitely large areas with subnanometre uniformity in periodicity. We demonstrate our approach through the fabrication of titanium dioxide and tungsten oxide nanostructures, but it can also be extended to a large variety of other materials.

The fabrication of nanostructures on surfaces is of paramount importance in nanotechnology and materials science[9]. There are several established techniques, including photolithography, electron-beam lithography, imprint lithography[10] and laser interference lithography[11], as well as non-conventional approaches such as self-assembly[12] and direct laser writing[13]. These techniques require either high-cost, complex systems or offer limited flexibility. An alternative flexible and potentially very low-cost method is laser-induced periodic surface structuring (LIPSS). The first observation of LIPSS dates back to 1965[14]. However, after almost 50 years and a large body of published work that has demonstrated LIPSS on various metals, semiconductors and glasses[15–19], the method has not found widespread use due to the stubborn problem of quality control[18,19].

Despite the evident role of self-assembly in the LIPSS process, uniformity and long-range order remain poor, a problem we identified as originating from the fact that the structures are initiated from multiple seed locations concurrently and independently, thereby producing an irregular pattern. Because the process is irreversible, without self-correction, these irregularities become frozen. Our solution to this relies on carefully exploiting feedback mechanisms to tightly regulate the formation of nanostructures induced by ultrashort pulses. This process can be summarized in three steps. (1) The laser beam, with a peak intensity close to the ablation threshold for titanium, is focused on a titanium surface, where it is scattered by existing nanostructures or any surface defects[15]. The interference of the scattered and incident fields leads to intensity variations in the immediate neighbourhood of the scattering point. (2) At points where the threshold intensity for ablation is exceeded, titanium reacts rapidly with O_2 from the air, forming titanium dioxide (TiO_2). The use of ultrashort pulses is necessary to ensure this process occurs faster than heat diffusion, as this can smear out the nanometre-scale localization of the deposited laser energy. The first two steps constitute a positive feedback loop (Fig. 1a). As the nanostructure grows, so does its scattering power. (3) The growth mechanism also has an imbedded negative feedback loop. As TiO_2 grows on top of the titanium, penetration of O_2 through the oxide layer decreases exponentially, decelerating and eventually halting the growth process (Fig. 1b).

The experimental set-up (Fig. 2 and Methods) consists of an ultrafast fibre laser[20] coupled to a microscope system for real-time observation of the nanofabrication process. All experiments were guided by a semi-phenomenological theoretical model developed by us. The main features of the model are summarized in the following and in the Methods, and the details are discussed in the Supplementary Information. Scattering of the incident laser field from a single point is modelled as dipole radiation[15,16], with the relative height of the surface point setting the scattering amplitude. This is confirmed experimentally (Fig. 3a) and numerically (Fig. 3b) by the structure formed around an isolated scatterer. The polarization of the laser sets the dipole radiation pattern, which results in regularly spaced nanolines parallel to the laser polarization. Circular polarization, which can be visualized as rotating linear polarization, results in an array of nanocircles. The period of the structures ranges between 600 and 900 nm, depending on the film thickness. Because the film is much thinner than the wavelength of light, light experiences a sort of a weighted average (effective) index of refraction which depends not only on that of the thin film, but also on those of the air and the substrate above and below the film, respectively. The total field at any surface point is the sum of the incident field and the total scattered field, which is given by the integral of the product of the surface height and the incident field over the entire surface. This surface integral is the mathematical origin of the nonlocal feedback. The amplitude of the dipole radiation decays with distance, which sets a finite range for this nonlocal feedback, such that two distant points on the surface have negligible mutual influence. For this reason, processing a large area at once results in structures with poor long-range order, as seen experimentally (Fig. 3c) and numerically (Fig. 3d). By limiting the size of the laser beam to ≲10 wavelengths, we ensure that even the most distant points under the beam have contributions to their mutual fields. This way, the problem of independent structure initiation is solved.

At points where the total intensity exceeds the ablation threshold ($\sim 1 \times 10^{12}$ W cm^{-2}), the metal (titanium) disassociates from the solid phase under the non-equilibrium conditions created by the ultrashort pulse and reacts with O_2 from the ambient atmosphere,

[1]UNAM—Institute of Materials Science and Nanotechnology, Bilkent University, 06800 Ankara, Turkey, [2]Department of Physics, Bilkent University, 06800 Ankara, Turkey, [3]Institute of Physics, National Academy of Science of Ukraine, Kiev, Ukraine, [4]Department of Micro and Nanotechnology, Middle East Technical University, 06800 Ankara, Turkey; [†]These authors contributed equally to this work. *e-mail: ilday@bilkent.edu.tr
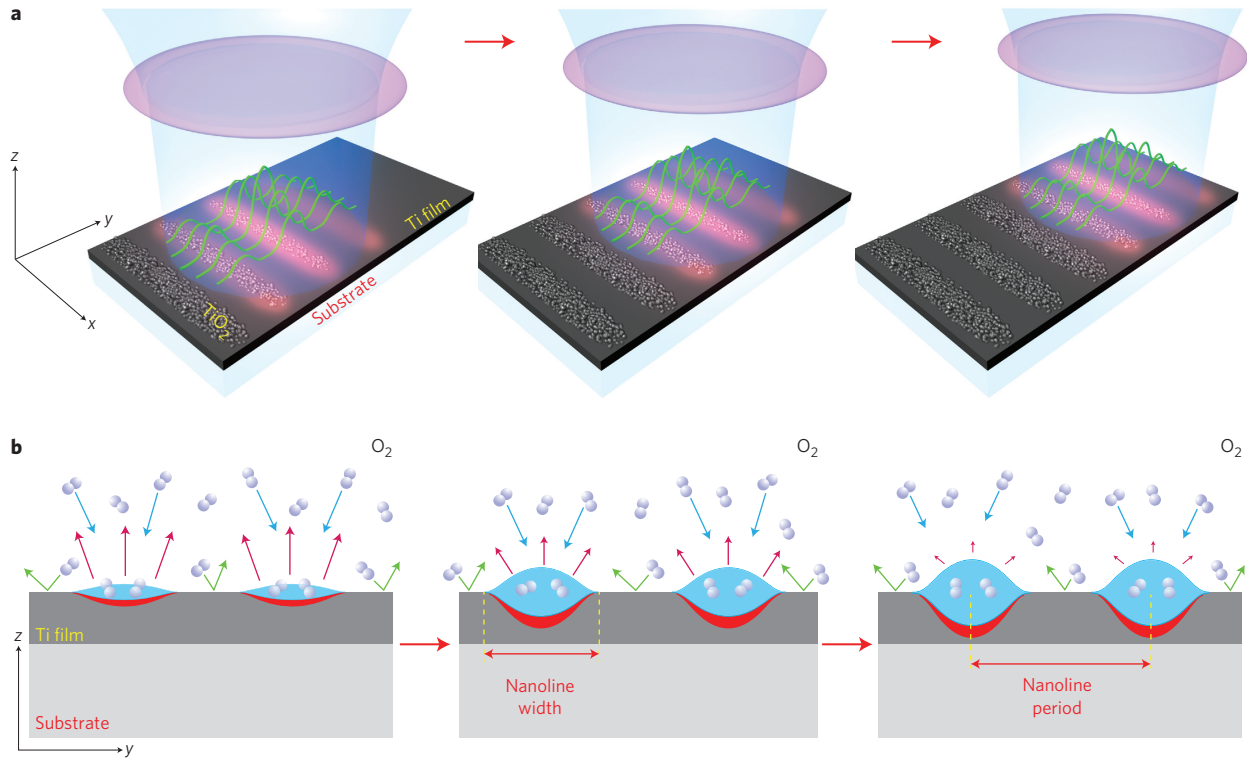
Figure 1 | Conceptual model. a, Schematic of the nanostructure formation process as a laser beam is scanned over the surface. **b**, Schematic showing a cross-sectional view of the surface, depicting the deceleration of the growth process due to negative feedback.
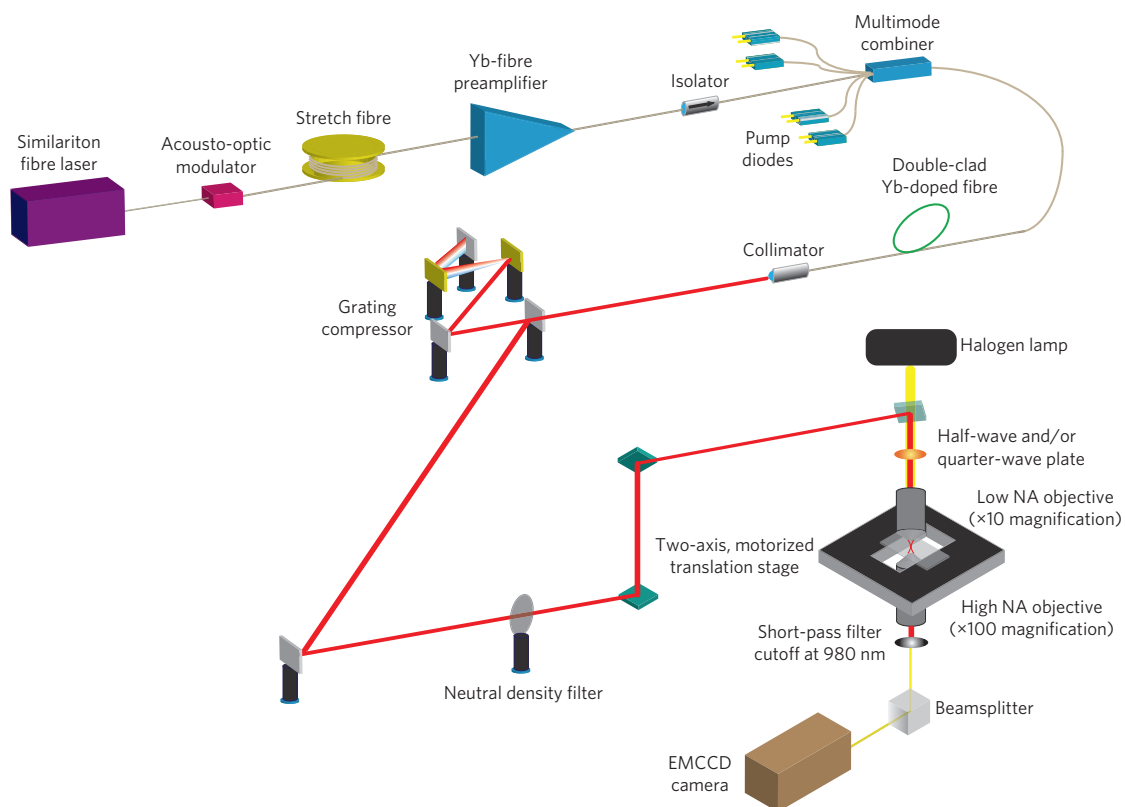
Figure 2 | Experimental set-up. An amplified fibre laser is coupled to a custom-built, computer-controlled optical microscope set-up. EMCCD, electron-multiplying charge-coupled device; NA, numerical aperture.
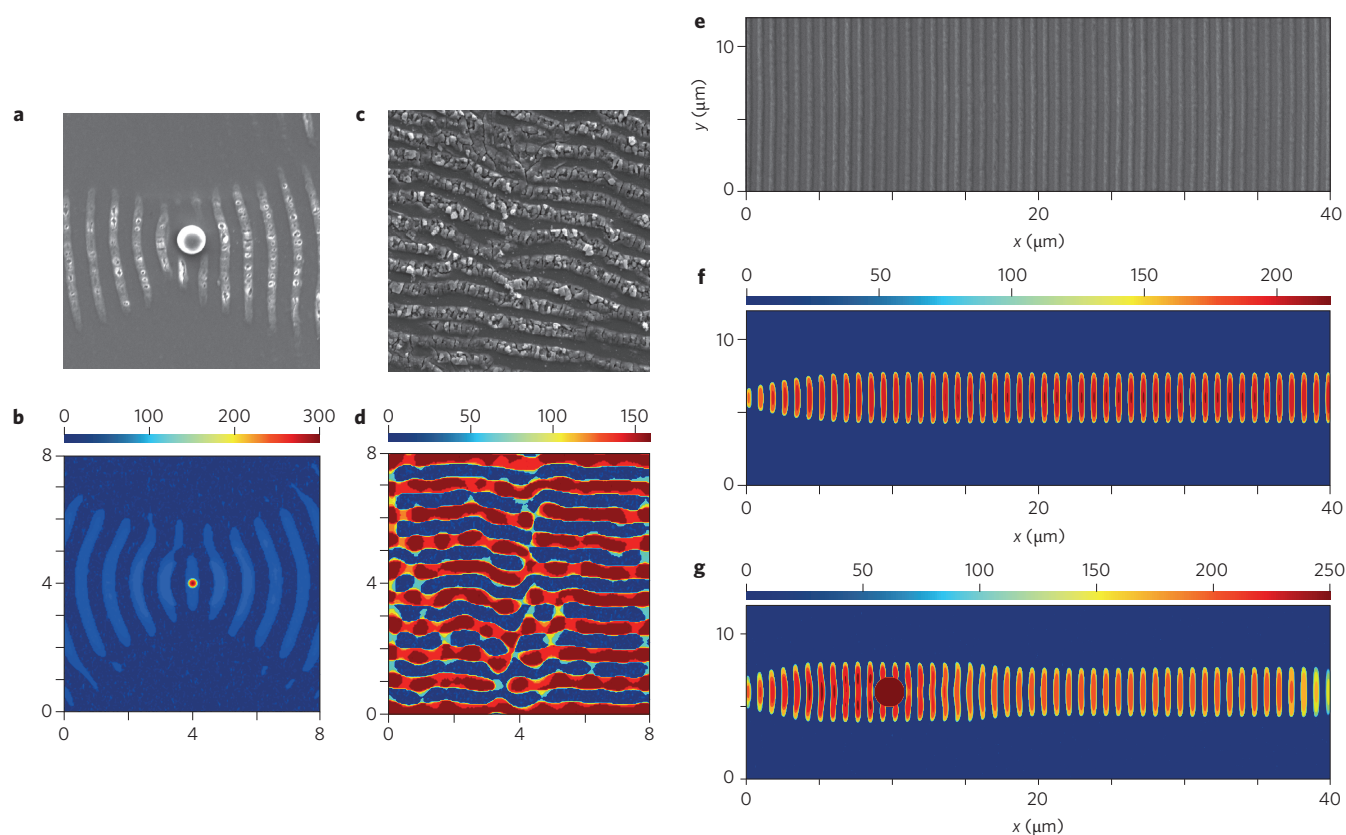
Figure 3 | Nanostructure formation dynamics. a,b, SEM image of the experimental results (**a**) and numerical simulation results (**b**) of nanostructures formed around an isolated scatterer by a few, high-energy pulses with linear polarization. **c,d**, SEM image of the experimental results (**c**) and numerical simulation results (**d**) of nanostructures obtained with a large and stationary laser beam. **e**, SEM image of uniform nanostructures obtained by scanning a small laser beam. **f**, Numerical simulation results of nanostructures obtained by scanning a small laser beam. **g**, Numerical simulation results showing robustness of the nanostructure formation against a defect, showing minor distortion and quick subsequent recovery. Colour bars indicate height in nanometres.

forming metal oxide (TiO_2) of an amount that is proportional to the laser-activated metal (titanium) or available O_2 at that point, whichever is smaller. Here, we simply refer to this controlled transformation as ablation, because similar physical processes underlie it, even though the metal is not removed, but is chemically transformed. As a result of the ablation threshold, no processing of the surface should occur between the nanolines, where partially destructive interference leads to the total intensity being below the ablation threshold. The presence of this threshold, which was confirmed experimentally (Fig. 3; Supplementary Section 'Experimental evidence for the threshold for intensity'), is the main source of nonlinearity.

When scanning a small-diameter beam, the nanostructures are created sequentially, with existing structures creating new structures, similar to the toppling of dominoes. This enables the formation of extremely uniform nanostructures (experimental and simulated results are shown in Fig. 3e and f, respectively). Moreover, it is possible to tile indefinitely large areas with nanostructures, without a discernible reduction in long-range uniformity when using a small laser beam. We scan the beam along a line, then shift the beam laterally while still preserving a partial overlap with the previous point, and then scan again parallel to the line of the scan (with partial overlap being maintained all along the way with the first line of the scan). This can be visually observed in Supplementary Movie S1, where the red disk represents the beam location and verified experimentally (Supplementary Movie S2). Further evidence of the role of nonlocal feedback lies in the fact that the new structures form a tilted front and the nanolines become distorted into a wavy pattern at the end of each scan line due to incomplete nonlocal feedback.

The nanostructure formation mechanism exhibits a significant degree of robustness against distinct types of perturbations. First, the resultant field at any point is formed collectively by the entire surrounding area, so the contributions of isolated defects or rough patches on the surface are easily overwhelmed. When a defect is placed along the beam path (under conditions otherwise the same as in Fig. 3f), the nanolines suffer only minor distortions (Fig. 3g). Defects encountered in Supplementary Movie S2 provide experimental confirmation. Second, Supplementary Movie S2 shows that the beam focus was not maintained well during scanning due to the poor mechanical stability of our set-up. However, key features, such as nanoline period and width, are independent of laser power (see Supplementary Section 'Insensitivity of the nanostructure features to laser power and exposure time' for direct experimental confirmation). Because of this insensitivity, a partial loss of focus during scanning is inconsequential. In fact, we found the standard and Allan deviations of the nanoline period of this structure to be 0.9 nm and 0.14 nm, respectively (for details see Supplementary Section 'Characterization of the uniformity of the nanostructures'). Third, as a result of the negative feedback mechanism, the growth of the nanostructures saturates at a given height. Even minutes-long exposure to a stationary beam or multiple scans of the laser over the same area have no discernible effect (Supplementary Movie S4). Robustness against a range of perturbations is a coveted feature of nonlinear systems[5] that is extremely difficult to achieve in strictly linear systems.

A diverse range of nanostructures have been fabricated using this approach. A photograph of nanostructures covering a 3 mm² area, fabricated on a thin and flexible glass slide, is presented in Fig. 4a.
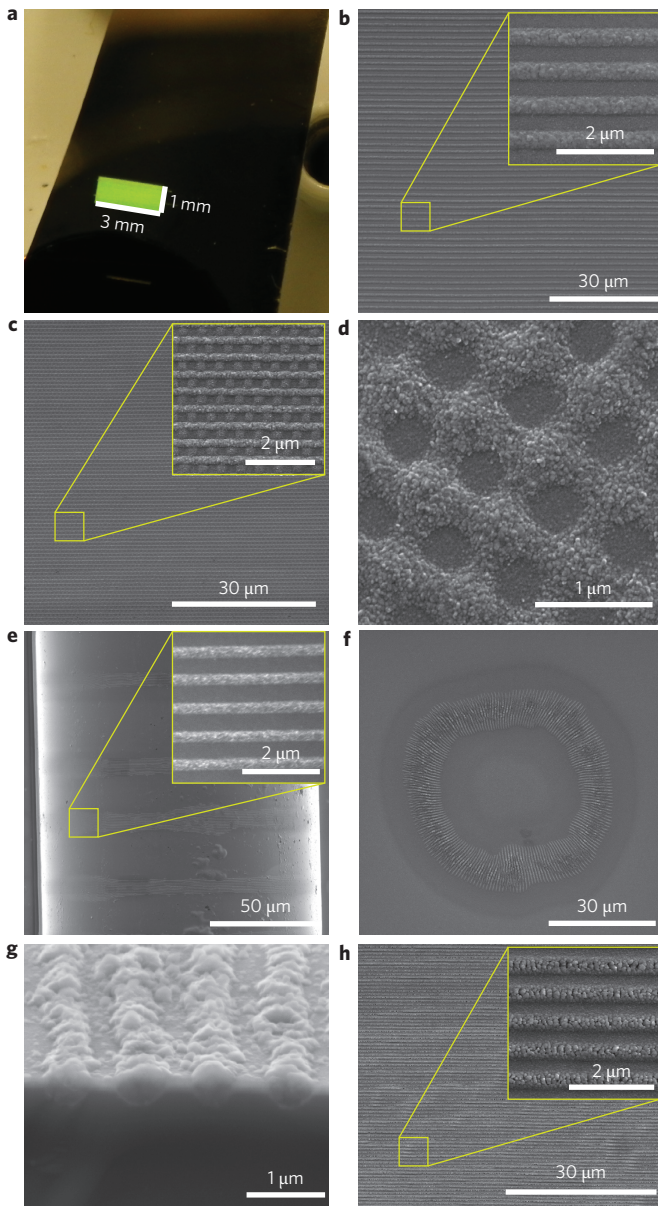
Figure 4 | Examples of fabricated nanostructures. a, Photograph of nanostructures covering an area of 1 mm × 3 mm (colouration is due to diffraction of room light). **b**, SEM image of a portion of the same structure. **c**, SEM image of mesh structure obtained by two scans of the beam with orthogonal polarizations. **d**, Nanocircles (diameter, 370 nm) obtained with circularly polarized light. **e**, Nanostructures fabricated on the side of a titanium-coated optical fibre, demonstrating the capability to fabricate on non-planar surfaces. **f**, Circular pattern of nanostructures obtained by rotation of the polarization direction. **g**, Cross-sectional SEM image of structures created on a thin film of titanium on a silicon substrate, showing imprinting of the nanostructures to the underlying substrate. **h**, Nanostructures obtained on a tungsten film over a glass substrate.

A scanning electron microscope (SEM) image of a section of the same structure is shown in Fig. 4b. A mesh structure of titanium dots surrounded by a mesh of TiO_2 is obtained by scanning with a linearly polarized beam, followed by a second pass with 90°-rotated polarization (Fig. 4c). Using circularly polarized light, a regular array of nanocircles is obtained (Fig. 4d, Supplementary Movie S4). An important advantage of this method is the capability to create these structures on non-planar surfaces due to the insensitivity of the process to variations in laser intensity. This is in clear contrast to conventional lithography techniques. As a demonstration, we scanned the beam over a titanium-coated optical fibre (125 μm diameter), creating structures despite the very strong surface curvature (Fig. 4e). Synchronously rotating the polarization during a circular scan results in optical resonator-like patterns (Fig. 4f), which could be interesting given the high index of TiO_2. The structures can be imprinted on a substrate such as silicon, where the titanium film is used only as a transfer material (Fig. 4g). If desired, titanium can be selectively etched afterwards. Although we focused on titanium in this work, our approach should be applicable to other materials. Indeed, Fig. 4h shows tungsten oxide structures fabricated on a tungsten surface.

To conclude, we report a simple, low-cost and high-speed method based on exploiting naturally occurring feedback mechanisms for the creation of metal–oxide nanostructures with femtosecond pulses. We have demonstrated periodic nanostructures covering areas measuring square millimetres with ~1 nm long-range uniformity on bulk and thin metal films on flexible substrates, as well as on the surface of an optical fibre, proving that non-planar surfaces can be processed. These special features, primarily the ability to process curved surfaces, are nominally not achievable with conventional techniques. In addition, our technique exhibits a substantial degree of robustness against defects and perturbations. This constitutes another demonstration that unique technological capabilities can emerge naturally by exploitation of nonlinear photonic systems[7]. Although we optimized the process for the oxidation of titanium and tungsten under a regular atmosphere, many metals, semiconductors and dielectrics have been shown to support LIPSS formation[15–19]. In principle, any of these materials can be subjected to a variety of chemical reactions under a suitable atmosphere to fabricate nanostructures from a virtually inexhaustible list of material compositions. The fabricated nanostructures can find applications in plasmonics[21], plasmonic nanolithography[22], photon detection[23], nanophotonics[24], memristors[25] and metallic nanostructures[26] for nanoelectronics, control of cell behaviour through patterned surfaces[27] and in low-cost fabrication of highly ordered TiO_2 structures, which have been shown to significantly increase the efficiency of dye-sensitized solar cells[28].

Methods

Laser set-up. The laser source was a home-built Yb-doped fibre laser, operating at a central wavelength of 1,060 nm and generating pulses with up to 1 μJ energy at 1 MHz, which can be compressed to 100 fs (ref. 20). The powers incident on the samples ranged from 100 mW to 1 W. The pulse-to-pulse power stability was on the order of 0.05% (measured from 3 Hz to 250 kHz).

Integrated laser microscope set-up. The pulses from the laser were coupled into a modified inverted microscope (Nikon Eclipse Ti) using a dichroic mirror with high reflectivity for 1 μm and high transmission of visible light. The focused spot size was set to ~12 μm (full-width at half-maximum intensity) in most experiments. Beam positioning was achieved by moving the sample on a dual-axis step-motor stage (Thorlabs, MAX203) with a repeatability of ~1 μm. The samples were illuminated with a halogen source, and imaging was carried out with a ×100 oil-immersion objective. The images were recorded with an electron-multiplying charge-coupled device camera (Andor, Luca).

Theoretical model. The semi-phenomenological three-step model was based on an integro-difference equation with decoupled timescales. The laser beam was modelled as a Gaussian beam centred at a point (x_0, y_0) on the surface. When the nth pulse of the pulse train was incident, it scattered from the surface protrusions and depressions, described by the local height of titanium, $h_n(x, y)$. The total laser intensity was calculated for every point (x, y) on the surface by integrating the contributions from the surrounding surface elements. Ablation occurs on a picosecond timescale, much faster than thermal diffusion, which would otherwise smear out the nanoscale localization of the absorbed laser energy. At points where the laser intensity exceeded the ablation threshold, titanium was ablated from its top surface down to the point where the intensity dropped below the ablation threshold. The amount of O_2 available was calculated based on the thickness of the TiO_2 layer at that point. Ablated titanium and O_2 react readily on a timescale much slower than the ablation process, but faster than the arrival of the next pulse (1 μs). The amount of TiO_2 formed was determined by the amount of ablated titanium and O_2, whichever was smaller. The surface profile was then updated as $h_{n+1}(x, y)$. The entire

process was repeated for the $(n + 1)$th pulse with an updated beam position (x_0, y_0). A full account of the model is given in Supplementary Section 'Detailed description of the theoretical model'.

References

1. Bhalla, U. S. & Iyengar, R. Emergent properties of networks of biological signaling pathways. *Science* **283,** 381–387 (1999).
2. Hopfield, J. J. Neural networks and physical systems with emergent collective computational abilities. *Proc. Natl Acad. Sci. USA* **79,** 2554–2558 (1982).
3. Ferrell, J. E. Jr. Self-perpetuating states in signal transduction: positive feedback, double-negative feedback and bistability. *Curr. Opin. Cell Biol.* **14,** 140–148 (2002).
4. Mandelbrot, B. How long is the coast of Britain? Statistical self-similarity and fractional dimension. *Science* **156,** 636–638 (1967).
5. Kitano, H. Biological robustness. *Nature Rev. Genet.* **5,** 826–837 (2004).
6. Haus, H. A. Theory of mode locking with a fast saturable absorber. *J. Appl. Phys.* **46,** 3049–3058 (1975).
7. Segev, M., Soljačić, M. & Dudley, J. M. Fractal optics and beyond. *Nature Photon.* **6,** 209–210 (2012).
8. Dudley, J. M., Finot, C., Richardson, D. J. & Millot, G. Self-similarity in ultrafast nonlinear optics. *Nature Phys.* **3,** 597–603 (2007).
9. Barth, J. V., Costantini, G. & Kern, K. Engineering atomic and molecular nanostructures at surfaces. *Nature* **437,** 671–679 (2005).
10. Ito, T. & Okazaki, S. Pushing the limits of lithography. *Nature* **406,** 1027–1031 (2000).
11. Sreekanth, K. V., Chua, J. K. & Murukeshan, V. M. Interferometric lithography for nanoscale feature patterning: a comparative analysis between laser interference, evanescent wave interference, and surface plasmon interference. *Appl. Opt.* **49,** 6710–6717 (2010).
12. Whitesides, G. M. Self-assembly at all scales. *Science* **295,** 2418–2421 (2002).
13. Gattass, R. R. & Mazur, E. Femtosecond laser micromachining in transparent materials. *Nature Photon.* **2,** 219–225 (2008).
14. Birnbaum, M. Semiconductor surface damage produced by ruby lasers. *J. Appl. Phys.* **36,** 3688–3689 (1965).
15. Temple, P. & Soileau, M. Polarization charge model for laser-induced ripple patterns in dielectric materials. *IEEE J. Quantum Electron.* **17,** 2067–2072 (1981).
16. Sipe, J. E., Young, J. F., Preston, J. S. & van Driel, H. M. Laser-induced periodic surface structure I: theory. *Phys. Rev. B* **27,** 1141–1154 (1983).
17. Bonch-Bruevich, A. M., Libenson, M. N., Makin, V. S. & Trubaev, V. V. Surface electromagnetic waves in optics. *Opt. Eng.* **31,** 718–730 (1991).
18. Sun, Q., Liang, F., Vallée, R. & Chin, S. L. Nanograting formation on the surface of silica glass by scanning focused femtosecond laser pulses. *Opt. Lett.* **33,** 2713–2715 (2008).
19. Bonse, J., Krüger, J., Höhm, S. & Rosenfeld, A. Femtosecond laser-induced periodic surface structures. *J. Laser Appl.* **24,** 042006 (2012).
20. Kalaycioglu, H., Oktem, B., Şenel, Ç., Paltani, P. P. & Ilday, F. Ö. Microjoule-energy, 1 MHz repetition rate pulses from all-fiber-integrated nonlinear chirped-pulse amplifier. *Opt. Lett.* **35,** 959–961 (2010).
21. Atwater, H. A. & Polman, A. Plasmonics for improved photovoltaic devices. *Nature Mater.* **9,** 205–213 (2010).
22. Srituravanich, W., Fang, N., Sun, C., Luo, Q. & Zhang, X. Plasmonic nanolithography. *Nano Lett.* **4,** 1085–1088 (2004).
23. Konstantatos, G. & Sargent, E. H. Nanostructured materials for photon detection. *Nature Nanotech.* **5,** 391–400 (2010).
24. Juan, M. L., Righini, M. & Quidant, R. Plasmon nano-optical tweezers. *Nature Photon.* **5,** 349–356 (2011).
25. Strukov, D. B., Snider, G. S., Stewart, D. R. & Williams, R. S. The missing memristor found. *Nature* **453,** 80–83 (2008).
26. Didiot, C., Pons, S., Kierren, B., Fagot-Revurat, Y. & Malterre, D. Nanopatterning the electronic properties of gold surfaces with self-organized superlattices of metallic nanostructures. *Nature Nanotech.* **2,** 617–621 (2007).
27. Flemming, R. G., Murphy, C. J., Abrams, G. A., Goodman, S. L. & Nealey, P. F. Effects of synthetic micro- and nano-structured surfaces on cell behavior. *Biomaterials* **20,** 573–588 (1999).
28. Kang, T.-S., Smith, A. P., Taylor, B. E. & Durstock, M. F. Fabrication of highly-ordered TiO$_2$ nanotube arrays and their use in dye-sensitized solar cells. *Nano Lett.* **9,** 601–606 (2009).

Author contributions

B.Ö. and I.P. conducted the experiments and analysed the data. I.P., S.I. and F.Ö.I. developed the theoretical model and I.P. performed the simulations. I.P., B.Ö., A.R., S.Y. and M.E. constructed the laser microscope set-up. H.K., B.Ö. and A.R. constructed the laser system.

Additional information

Supplementary information is available in the online version of the paper. Reprints and permissions information is available online at www.nature.com/reprints. Correspondence and requests for materials should be addressed to F.Ö.I.

Competing financial interests

The authors declare no competing financial interests.

SUPPLEMENTARY SECTION

Nonlinear Laser Lithography for Indefinitely Large Area Nanostructuring with Femtosecond Pulses

Bulent Öktem[1], Ihor Pavlov[2,3], Serim Ilday[4], Hamit Kalaycıoğlu[2], Andrey Rybak[2,3], Seydi Yavaş[1], Mutlu Erdoğan[1], and F. Ömer Ilday[2]

[1] UNAM – Institute of Materials Science and Nanotechnology, Bilkent University, 06800, Ankara, Turkey

[2] Department of Physics, Bilkent University, 06800, Ankara, Turkey

[3] Institute of Physics, National Academy of Science of Ukraine, Kiev, Ukraine

[4] Department of Micro and Nanotechnology, Middle East Technical University, 06800, Ankara, Turkey

Detailed description of the theoretical model

The incident pulse train is modelled as a Gaussian beam along the z axis and normally incident on the surface, which lies in the (x,y) plane at $z=0$. The local height (in nm) of the metallic surface, $h(x,y)$, is nominally initially set to $h(x,y)=\delta(x,y)\Delta h$, where $\delta(x,y)$ is a random variable with an average value of zero and root-mean-square (rms) value of 1. Δh characterises the rms roughness of the surface.

$$I_{inc}(x,y,t)=\sum_n I_n(x,y,t), \tag{1}$$

$$I_n(x,y,t)=I_0\exp\left[-\frac{(x-x_{0,n})^2+(y-y_{0,n})^2}{w^2}-\frac{(t-nT_R)^2}{\tau_p}\right]. \tag{2}$$

Here, n is the pulse number, $(x_{0,n},y_{0,n})$ determine the centre of the beam, which is slowly (compared to T_R) shifting if the beam is being scanned over the surface, w is the beam width, T_R is pulse-to-pulse separation, and τ_p is the pulse width. For typical scanning speeds we have utilised, up to 1 million pulses are incident at a point on the surface.

The interaction of a laser with a metal target is largely independent of the pulse shape and even of the duration for pulse durations in the sub-picosecond regime[1,2]. Consequently, we simplify the description that follows by assuming the pulse to be of square shape and drop the explicit time dependence. The corresponding electric field of the beam within the pulse duration for arbitrary polarisation is given by

$$\vec{E}_n(x,y)=(E_x\hat{x}+E_ye^{i\phi}\hat{y})e^{-\frac{(x-x_{0,n})^2+(y-y_{0,n})^2}{2w^2}}. \tag{3}$$

Here, we have chosen the units such that $I_n=\left|\vec{E}_n\right|^2$.
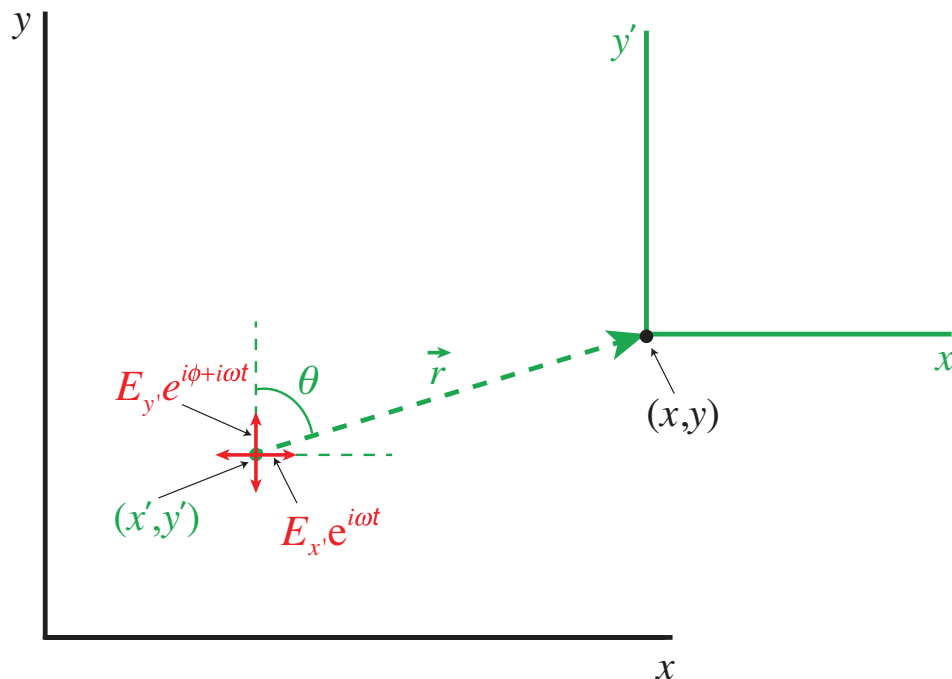
Figure S1. Coordinate system used in calculating the amplitude of the scattered electric field at a point (x,y) due to a surface element at coordinate (x',y'). To calculate the total scattered field at (x,y), it is necessary to integrate over all (x',y').

We consider the scattered field from a single defect to be dipole-like. The amplitude of the scattered electrical field at point (x,y) on the surface, due to a surface element at coordinate (x',y') (Fig. S1) is given by

$$\vec{E}_{scat}(x',y') = \left\{ \begin{array}{l} \left[E_{x'}(g_\theta \cos^2\theta - f_r \sin^2\theta) + E_{y'}\,e^{i\phi}\sin\theta\cos\theta(f_r + g_\theta) \right]\hat{x}' \\ + \left[E_{x'}\sin\theta\cos\theta(g_\theta - f_r) + E_{y'}\,e^{i\phi}(f_r\cos^2\theta + g_\theta\sin^2\theta) \right]\hat{y}' \end{array} \right\} \times e^{-\frac{(x'-x'_{0,n})^2+(y'-y'_{0,n})^2}{2w^2}}. \quad (4)$$

In addition, we have

$$f_r = 2\xi h(x',y')\left(\frac{1}{r^2} - \frac{i}{kr^3} \right)e^{i(\omega t - kr)}, \quad (5)$$

$$g_\theta = \xi h(x',y')\left(\frac{k}{r} - \frac{i}{r^2} - \frac{1}{kr^3} \right)e^{i(\omega t - kr)}, \quad (6)$$

where ξ is a proportionality coefficient, $h(x',y')$ is the local height of the metallic surface at coordinates (x',y'), and $k = 2\pi / \Lambda$ is the wave number of the scattered wave, $\hat{x}'(\hat{y}')$ is the unit

vector along the $x'(y')$ axis, θ is the angle between $\vec{r}$ and $\hat{y}'$, and $\vec{r}$ is the displacement vector between (x, y) and (x', y'). In order to find the total local field at an arbitrary point (x, y) on the surface, we integrate over the contributions from all points on the surface,

$$\vec{E}_{surf,n} = \vec{E}_n(x, y) + \iint \vec{E}_{scat}(x', y') dx' dy'. \tag{7}$$

Here, normalization of this result to ensure that the sum of the total power scattered over the surface and that of the reflected light equals the incoming power is implicit.

In order to clarify the underlying physics, let us consider the special case of linearly polarised light along the y axis. As such, $\phi = 0$, $E_{x'} = 0$ and $E_{y'} = E_0$. Then, our result reduces to

$$\vec{E}_{scat}(x', y') = E_0 \left\{ \sin\theta \cos\theta (f_r + g_\theta)\hat{x}' + (f_r \cos^2\theta + g_\theta \sin^2\theta)\hat{y}' \right\} \times e^{-\frac{(x'-x'_{0,n})^2 + (y'-y'_{0,n})^2}{2w^2}}.$$

For large r, further simplification is in order,

$$\vec{E}_{scat}(x', y') = \left\{ E_{y'} e^{i\phi} g_\theta \sin\theta \cos\theta \hat{x}' + E_{y'} e^{i\phi} g_\theta \sin^2\theta \hat{y}' \right\} \times e^{-\frac{(x'-x'_{0,n})^2 + (y'-y'_{0,n})^2}{2w^2}}$$

$$= E_0 \exp\left(-\frac{(x'-x'_{0,n})^2 + (y'-y'_{0,n})^2}{2w^2} \right) \xi h(x', y') \left(\frac{k}{r} \right) \sin^2\theta \, e^{i(\omega t - kr)} \hat{y}'. \tag{8}$$

Thus, the total electric field and intensity formed on the surface during the nth pulse reduce to

$$E_{surf,n}(x, y) = \underbrace{E_n}_{\substack{n \text{ is} \\ \text{the pulse} \\ \text{number}}}(x, y) + \xi \iint E_0 \underbrace{h(x', y')}_{\substack{\text{effect of the} \\ \text{surface point}}} \underbrace{\left(\frac{k}{r} \right)}_{\substack{\text{sets the finite} \\ \text{range of influence}}} \underbrace{\sin^2\theta}_{\substack{\text{determines} \\ \text{direction of} \\ \text{nanostructures}}} \underbrace{e^{i(\omega t - kr)}}_{\substack{\text{phase term,} \\ \text{where } k \\ \text{determines} \\ \text{the period}}} \underbrace{e^{-\frac{(x'-x'_{0,n})^2 + (y'-y'_{0,n})^2}{2w^2}}}_{\substack{\text{imposes the finite-size} \\ \text{of the laser beam}}} dx' dy', \tag{9}$$

$$\underbrace{\phantom{E_{surf,n}(x, y) = E_n(x, y) + \xi \iint E_0 h(x', y')}}_{\text{integration over the entire } (x, y) \text{ plane}}$$

$$I_{surf,n}(x, y) = \left| E_{surf,n}(x, y) \right|^2, \tag{10}$$

where we have ignored the component along $\hat{x}'$, since it does not interfere with the incoming light, which is along $\hat{y}'$ and the implicit normalisation operation suppresses its influence.

Interpretation of this result is straightforward. The total field is a surface integral with the product of the surface height and the incident field at each point contributing. The form of the integral is

suggestive of an interpretation as a Fourier integral over the surface height, $h(x',y')$, albeit with important differences. First, there is a preferred direction due to the $\sin^2\theta$ term, which sets the direction of the nanolines to be parallel to the polarisation direction. Second, the contribution of each scattering point decays with r^{-1}. This effectively sets sort of a coherence range; two regions of the surface, some sufficiently large distance away from each other, can have no influence on each other, but each region will contribute to nanostructure formation in its immediate vicinity (Fig. S2). This is the mechanism through which concurrent and independent nanostructure formation occurs when large spot sizes are used and it must be prevented to achieve a globally ordered structure, which we accomplish by restricting the spot size on the surface: The envelope of the beam, $\exp[-\{(x-x_{0,n})^2+(y-y_{0,n})^2\}/2w^2]$, also appears in the integrand, which effectively sets the upper range of the integral since near the edge of the beam the laser intensity will be lower than the minimum intensity required to activate the surface. This is a key point, through which we ensure that during each pulse, every single point illuminated by the laser beam contributes to the total field at every other point. Finally, the e^{ikr} term imposes the periodicity of the nanostructures.
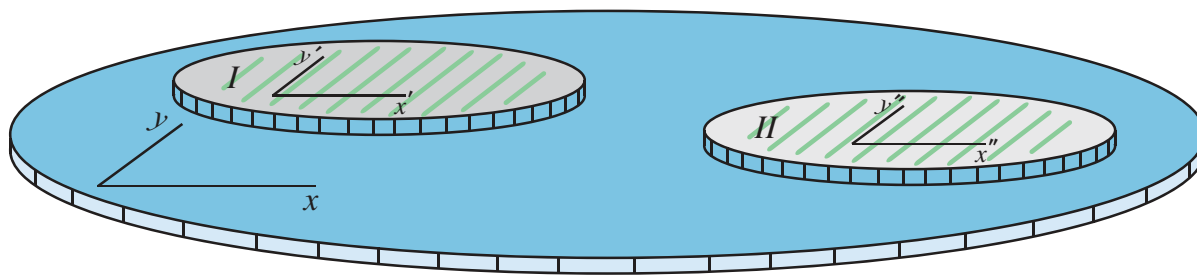
Figure S2. Cartoon showing two regions, Region I and Region II, which contribute to the formation of nanostructures in their immediate vicinity, but which are far apart enough that they have no mutual influence, resulting in concurrent, but independent growth of the nanostructures.

Next, we formulate the chemical reaction between the metallic surface and oxygen from the air, which leads to the production of the metal-oxide. Light intensity reaching a planar slice of thickness dz, at a depth z below the surface, is given by

$$I_n(x,y,z) = I_{surf,n}(x,y)e^{-z/z_s}, \tag{11}$$

where z_s is the skin depth of the metal (Ti). The ablated volume element of Ti below the surface corresponding to a differential area of dA is given by

$$dV(x,y) = dA \int \alpha(x,y,z)dz, \tag{12}$$

where $\alpha(x,y,z)$ is the probability of ablation, which depends on the laser intensity. As a simplifying approximation, we assume that the ultrafast ablation of the metal (*e.g.*, Ti) surface occurs only if the deposited energy per unit area (fluence) exceeds the threshold for this process. This is justified for few-picosecond and shorter pulse durations[1,2]. Here, we use the term *ultrafast ablation* to refer to disassociation of the Ti from solid form under non-equilibrium conditions created by the use of energetic, ultrashort pulses. Thus, for a given pulse duration, τ_p, there is a corresponding threshold peak intensity, I_{th}, which must be exceeded. For intensities below this critical level, no ablation occurs. Consequently,

$$\alpha(x,y,z) = H(I_n(x,y,z) - I_{th}), \tag{13}$$

where $H(x)$ is the Heaviside function.

We assume, for simplicity, that the metal-oxide (TiO$_2$) synthesis is directly proportional to the amount of free (ablated) metal (Ti) and O$_2$ at that point in space. Therefore, the volume element ablated by the nth pulse at point (x,y) on the surface is given by

$$dV(x,y) = dA\Delta z_n, \text{ and}$$

$$\Delta z_n(x,y) = \begin{cases} z_s \ln(I_{surf,n}(x,y)/I_{th}) & \text{for } I_{surf,n}(x,y) > I_{th} \\ 0 & \text{for } I_{surf,n}(x,y) < I_{th} \end{cases}. \tag{14}$$

The number of evaporated Ti atoms at any point of surface is given by

$$N_{Ti}(x,y) = dV(x,y)\rho N_A / M_{Ti}, \tag{15}$$

where ρ is the density of Ti, M_{Ti} is the molar mass, and N_A is the Avogadro's number. In the calculation of I_{th}, we neglect energy transfer from the evaporated volume to the surrounding region, which is justified for pulses shorter than a few picoseconds. Accordingly, the amount of energy that needs to be absorbed per volume element, dV, to provide the energy for ablation, is approximately given by $dW = \rho L dV$. Here, L is an effective total heat capacity for Ti for ablation, which includes energy required for heating, as well as the latent heat capacities for melting and evaporation.

The amount of absorbed fluence is given by $W_{abs} = I_{surf,n} \tau_p \left(1 - e^{-z/z_s} \right)$, from which we estimate the energy that must be absorbed within a thin slice to achieve ablation as

$$dW_{abs} = I_{surf,n} \frac{\tau_p}{z_s} e^{-z/z_s} dz dA, \tag{16}$$

The minimum intensity for ablation on the surface should be,

$$I_{th} = \rho L z_s / \tau_p, \tag{17}$$

For Ti, using $z_s = 30 \text{ nm}$, $L = 11500 \text{ J/g}$, $\rho = 4500 \text{ kg/m}^3$, and $\tau_p = 170 \text{ fs}$, we obtain $I_{th} = 1 \times 10^{12} \text{ W/cm}^2$, corresponding to a fluence of 0.17 J/cm^2, which agrees well with published ablation thresholds for Ti with sub-picosecond pulses[3,4]. The experimentally determined threshold value for the incident fluence per pulse is $\sim 0.1 \text{ J/cm}^2$, the value of which depends weakly on the surface roughness. Given the simplicity of this model, the agreement is considered to be good.

As for the amount of oxygen molecules available to react with Ti, we assume that this number is decreasing exponentially with the thickness of the titanium dioxide layer that forms on top of the evaporated Ti and acts as a barrier. We formulate this as

$$N_{O_2} = C_1 e^{-h'(x,y)/h_c}, \tag{18}$$

where C_1 is a proportionality constant, $h'(x,y) = \eta h(x,y)$ is the height of TiO$_2$ layer, which is related to the height of the Ti layer, $h(x,y)$, by a proportionality constant, η, and h_c is a critical thickness parameter, which characterises the extend of diffusion of O$_2$ into TiO$_2$.

The number of TiO$_2$ molecules produced after every pulse is highly dependant on the partial pressures of the reactants, Ti and O$_2$. Lack of availability of the either of the reactants will halt further production of TiO$_2$. In other words, the number of TiO$_2$ molecules formed cannot exceed the number of ablated Ti atoms, or the number of O$_2$ molecules present at that point, whichever is smaller. Therefore, quite simply,

$$N_{TiO_2} = N_{Ti}, \text{ if } N_{Ti} < N_{O_2}, \text{ or}$$
$$N_{TiO_2} = N_{O_2}, \text{ if } N_{Ti} > N_{O_2}. \tag{19}$$

The change in height through the action of by the nth pulse at point (x,y) on the surface is taken to be proportional to the number of TiO$_2$ molecules,

$$\Delta h_n(x,y) = C_2 N_{TiO_2}. \tag{20}$$

We take $\xi = 10^{-3}$ m, $C_2 = 1720$ m, and incident wave peak intensity to be 1×10^{12} W/cm^2, which is similar to the calculated value of I_{th}.

Once the calculation of the effect of the nth pulse is finished, the process is repeated for the by the $n+1^{th}$ pulse with the updated values of $(x_{0,n+1}, y_{0,n+1})$, if the beam is being scanned and with the updated values of E_x, E_y, and ϕ, if the polarisation is changed.

Even though the theoretical model we have developed is semi-phenomenological, the numerical simulations based on this model form the core of our physical understanding and have guided the experimental development of nanostructures towards achievement of unprecedented levels of uniformity. Furthermore, the model predicts all the salient features observed experimentally. We

find that the exact details of the formulation do not change the qualitative nature of the results and influence only the details, as long as several essential features of the model are retained. In the remaining sections, each of these essential features and the important results of our model are discussed further and compared to experimental results.

Modulational instability of a flat surface beyond critical laser intensity

The spontaneous formation of nanostructures under the influence of the laser beam needs to be explained theoretically. As one can see from our model even by inspection, a perfectly flat (*i.e.*, defect-free) surface is a state of equilibrium state as the laser field intensity will be uniform over the surface. However, this does not necessarily mean that this state is stable against defects (or surface roughness). Here, we show that a flat surface becomes unstable in the presence of a single infinitesimal defect if the laser intensity exceeds a critical value. This situation is of similar nature to various physical systems, including modulational instability in the context of solitons[5].

In order to simplify the problem, we consider a toy model for a 1D surface, *i.e.*, a line, since the generalisation of the main results of this section to a 2D surface is straightforward, but complicated. Let the height of the surface be given by

$$h(x) = h_0 + \delta(x - x_0)\Delta h \qquad (21)$$

i.e., an otherwise perfectly flat surface, but with a single defect of height, Δh, located at $x = x_0$. In 1D, the total electric field is given by

$$E_{surf,n}(x) = E_0 + \xi \iint E_0 h(x') \frac{k}{|x - x'|} e^{-ik|x-x'|} dx'$$

$$= E_0 + \xi \iint E_0 [h_0 + \Delta h \delta(x' - x_0)] \frac{k}{|x - x'|} e^{-ik|x-x'|} dx'$$

$$= E_0 \left(1 + \xi \Delta h \frac{k}{|x - x_0|} e^{-ik|x-x_0|} \right), \qquad (22)$$

9

where we have assumed that the beam width on the surface is extremely large (plane wave limit), since our interest is in the stability of the surface. The component of the integral over h_0 vanishes due to symmetry. Assuming the defect on the surface is small, we proceed with a linearized stability analysis.

$$I_{surf,n}(x) = I_0 \left| 1 + \xi\Delta h \frac{k}{|x-x_0|} e^{-ik|x-x_0|} \right|^2 = I_0 \left(1 + 2\xi k\Delta h \frac{e^{-ik|x-x_0|}}{|x-x_0|} + O\left(\Delta h^2\right) \right), \qquad (22)$$

after which we will keep only the first-order term in Δh. Similar to the previous section, the ablation depth for our hypothetical 1D surface will be given by,

$$\Delta z_n(x) = \begin{cases} z_s \ln(I_{surf,n}(x)/I_{th}) & \text{for } I_{surf,n}(x) > I_{th} \\ 0 & \text{for } I_{surf,n}(x) < I_{th} \end{cases}. \qquad (23)$$

Initially, the surface is flat, except for the small defect point. Thus,

$$z_s \ln\left[I_0/I_{th}\left(1 + 2\xi k\Delta h \frac{e^{-ik|x-x_0|}}{|x-x_0|} \right) \right] = z_s \left[\ln(I_0/I_{th}) + 2\xi k\Delta h \frac{e^{-ik|x-x_0|}}{|x-x_0|} + O\left(\Delta h^2\right) \right] \qquad (24)$$

Clearly, we have, to a good approximation,

$$\Delta z_n(x) = \begin{cases} z_s \ln(I_0/I_{th}) + 2z_s\xi k\Delta h \dfrac{e^{-ik|x-x_0|}}{|x-x_0|} & \text{for } I_0 > I_{th} \\ 0 & \text{for } I_0 < I_{th} \end{cases}. \qquad (25)$$

This result shows that there will be no change at any point on the surface unless $I_0 > I_{th}$ if Δh is sufficiently small. An important corollary of this result is that for a sizeable defect, the laser threshold for nanostructure formation is less I_{th}, which is consistent with our experimental observation that the laser threshold for nanostructure formation is significantly reduced, when starting around an existing defect. The result obtained from our toy model is valid for $k|x-x_0| > 1$. Nevertheless, it is capable of illustrating the relevant physics. The most relevant case is when the peak intensity is very close to the threshold intensity, in which case we have the changing in surface height as follows,

$$\Delta h_n(x) = \eta \Delta z_n(x) = \begin{cases} 2z_s \eta \xi k \Delta h \dfrac{e^{-ik|x-x_0|}}{|x-x_0|} & \text{for } I_0 \gtrsim I_{th} \\ 0 & \text{for } I_0 < I_{th} \end{cases} . \tag{26}$$

Here, we have recognized that the ablated metal structure will be fully converted (within a proportionality constant, η) to a change in metallic surface height, since saturation due to oxygen unavailability can be safely neglected for a defect of infinitesimal size. This result shows, very importantly, that an isolated defect leads to growth at adjacent peaks separated by the period, $\Lambda = 2\pi/k$ (Fig. S3). When the next pulse arrives, the two slightly larger defects formed immediately on either side of the original defect by the first pulse will both contribute to further growth of the original defect, as well as their own neighbours. Since the growth rate is proportional to the size of the defect, Δh, growth is exponential (positive feedback) until saturation kicks in.

In summary, our toy model for 1D demonstrates the important result that a flat surface is unstable against infinitesimal defects, if $I_0 \gtrsim I_{th}$. The instability is strongly reminiscent of modulational instability in nonlinear optics. In addition, the fact that growth occurs at adjacent peaks separated by Λ is a key result, demonstrating the non-local, yet periodic nature of the positive feedback and consequently, the spontaneous emergence of the periodicity of the nanostructures.
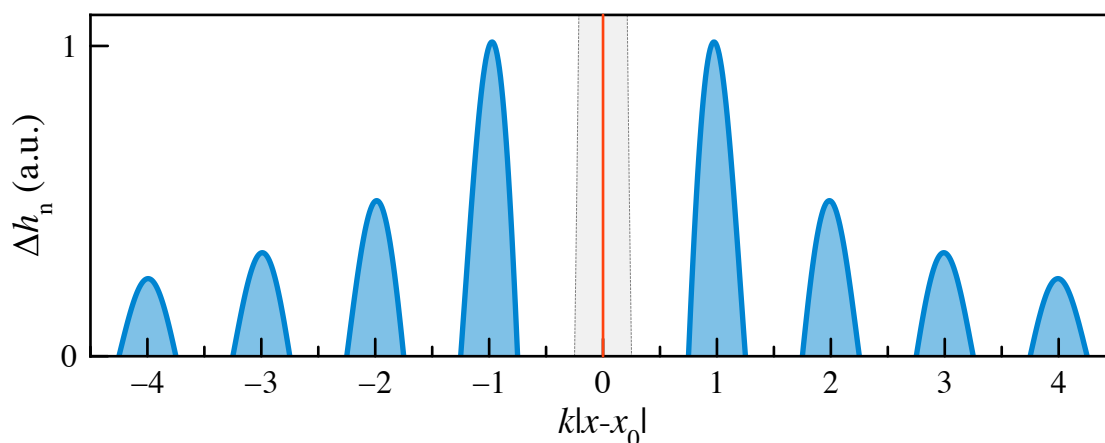
Figure S3. Plot of change in surface height after one pulse as a function of position along the 1D surface. Red line represents the location of the infinitesimal defect, $\delta(x-x_0)\Delta h$.

Numerical simulations clearly show that the full model corresponding to a 2D surface exhibits modulation-instability-like behaviour for a perfectly flat surface with just a single defect. This is consistent with our experimental experience that the better polished the surface is, the higher laser intensity needed to start the nanostructure formation (i.e., if Δh is small, the minimum required laser intensity is higher). As expected, once the first structures are formed, the laser intensity can be reduced to values significantly less than the value required to initiate the nanostructure formation.

Experimental evidence for the threshold for intensity

The nonlinear characteristic of the process is evident from the existence of a sharp threshold in intensity for the formation of TiO_2 structures. In laser interference lithography, material modification occurs through linear absorption of (typically UV) light in a photoresist material. There is no power threshold for this process and the volume of material processed is essentially a linear function of the laser intensity. Therefore, the intensity determines the rate of the chemical transformation. However, there is no on/off mechanism and at points with partially destructive interference, the process is simply slower. Consequently, an interference pattern can easily be erased through over exposure. In our case, however, no processing occurs at surface points, where the intensity is below a critical value. Therefore, the pattern will not change once it is formed, even with indefinitely long exposure. There is no possibility of over exposure; once the nanopattern has formed, spatial points with intensity below the threshold will no longer be affected. This can be visually seen in the experimental movies, when the beam is not moving. The complete lack of processing of the surface in the troughs, between the peaks is demonstrated by experiments done on bulk Ti samples. Some of these samples had shallow surface scratches, which were determined to be 10-20 nm in depth by atomic force microscope (AFM) analysis. We have observed that these scratches are perfectly preserved in between the nanolines (Figure S4), proving the complete

absence of laser-induced TiO_2 formation at these points, and confirming the existence of a sharp threshold on local intensity.
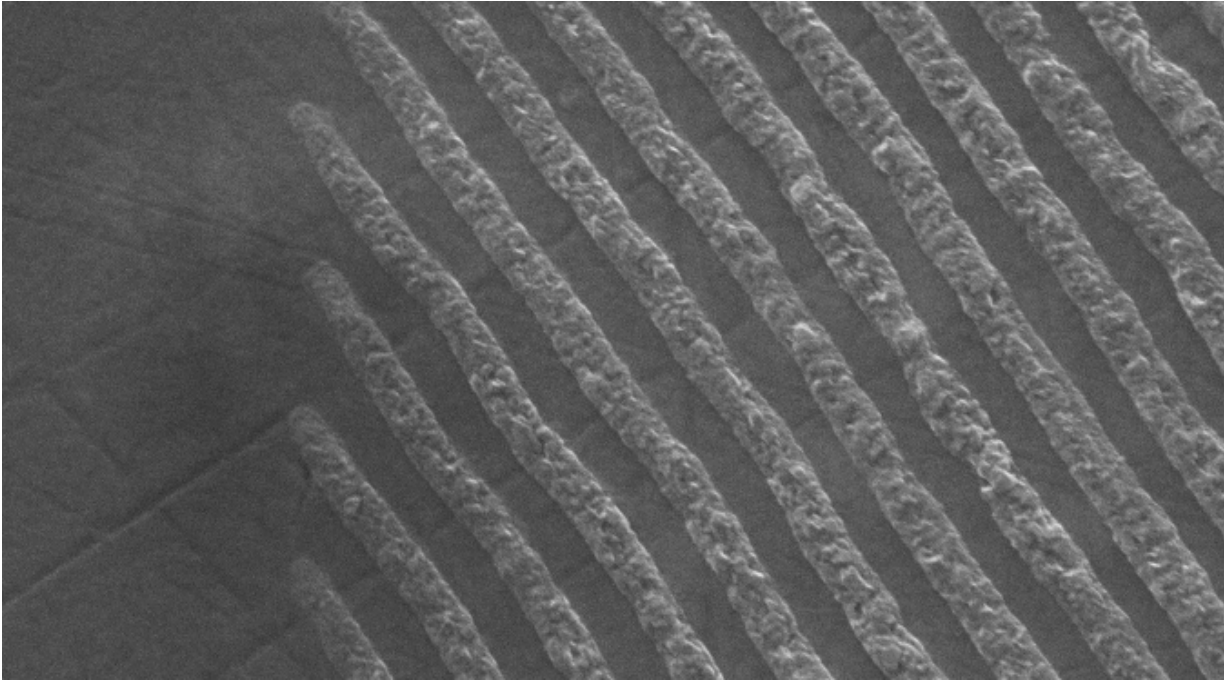

Figure S4. Pre-existing scratches on surface are preserved between the nanolines. SEM image of nanolines showing continued existence, after nanostructure formation, of a pre-existing crack on the surface. According to AFM analysis, the depth of these cracks range between 5-20 nm.

The existence of an intensity threshold and absence of possibility of overexposure is an essential difference from linear laser interference lithography that stems directly from the nonlinear nature of the process.

The role of nonlocal positive feedback

The positive feedback that arises from the surface integral in Equation (9) can easily be visualised through numerical simulations. Fig. S5a illustrates nanostructures formed by scanning a laser beam over the surface, which constitutes a snapshot in the numerical simulations shown in Supplementary Movie 1. Fig. S5b shows the contributions to the field formation at a specific point marked in Fig. S5a. The contributions, corresponding to the kernel of Equation (9), arise from the

entire area surrounding the point, which underlies the built-in robustness of the nanostructure formation mechanism: The contributions of a reasonably small defect will always be overwhelmed by a much larger surrounding area.
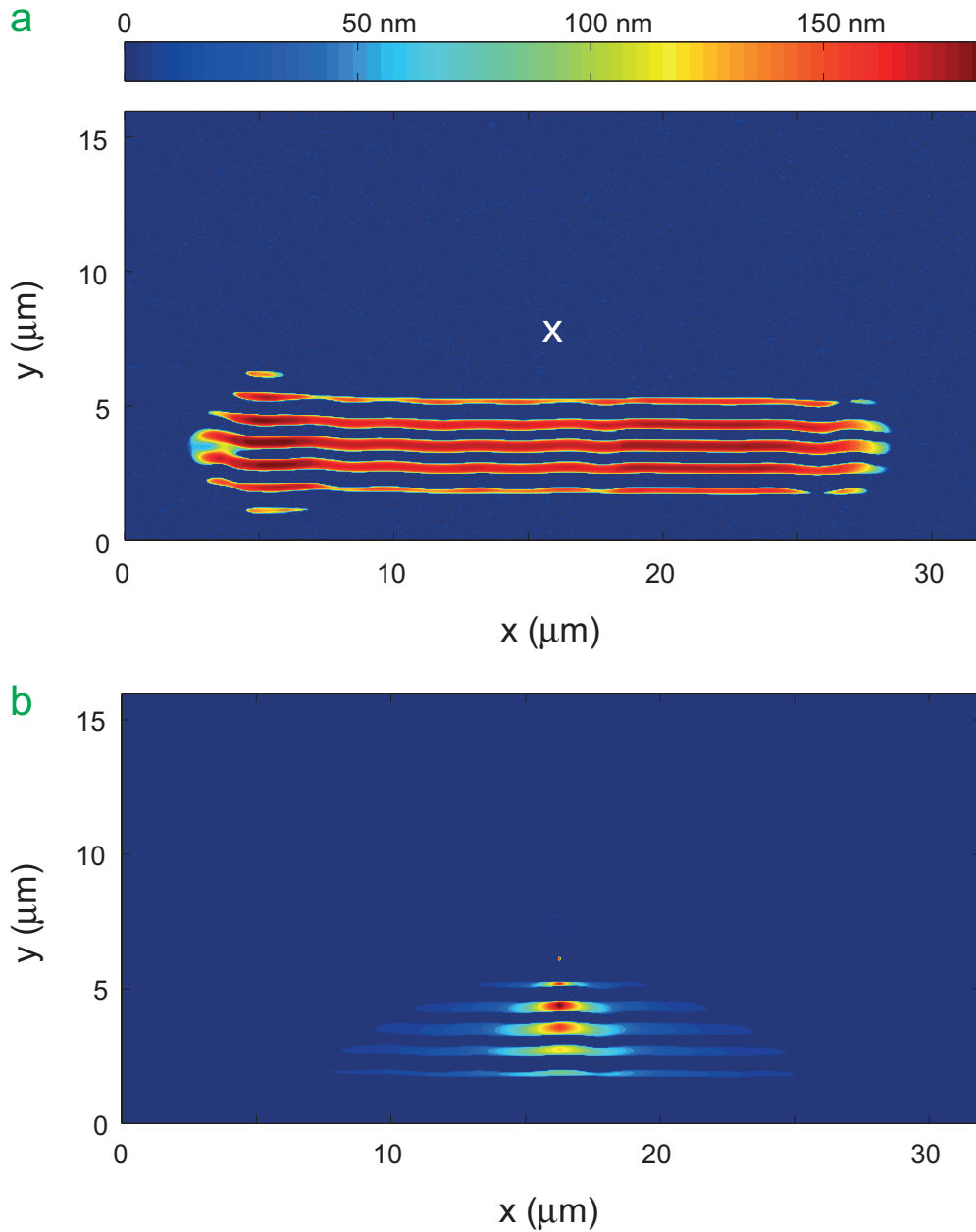
Figure S5. (a) Numerically simulation of formation of nanostructures. The white cross denotes the point for which the electric field is calculated. **(b)** Contribution to the field at the point marked with the white cross from the surrounding area.

14

Saturation of growth due to negative feedback

The negative feedback that arises due to the increased difficulty of oxygen reaching the ablated Ti structures as the TiO_2 structure grows is responsible for the halting of the growth process. We model oxygen available to be decreasing exponentially with increasing thickness of the TiO_2 layer. Therefore, the growth of the height of the structures should increase only logarithmically with the number of incident pulses. The numerical simulations confirm this behaviour (Fig. S6). Simulations are carried out only to 1000 pulses due to excessive computational time required to continue further.
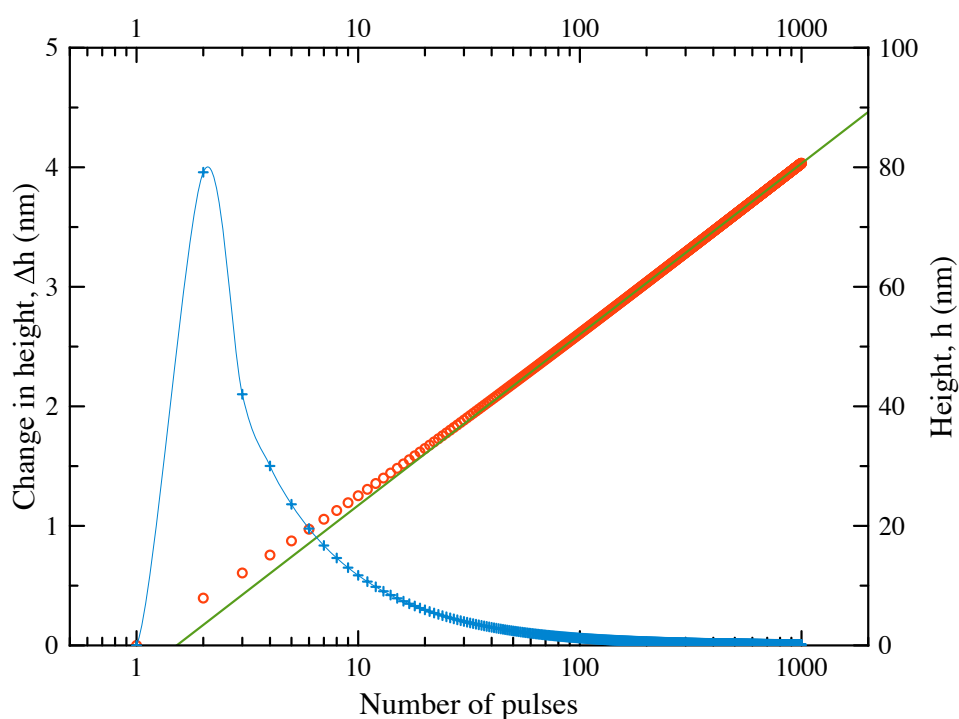
Figure S6. Results of numerical simulations showing total height (red circles) and change in height after each pulse (blue crosses). Green line shows logarithmic fit, which is valid in the deep saturation limit. In experiments, typically around 10^6 pulses are incident on each spot.

Experimental evidence comes from the videos, which show clearly that even when the beam is stationary for tens of seconds, during which more than 10^7 pulses are incident on the surface, the existing structure remains unchanged. This confirms that even a very large number of pulses leads

15

to no further processing, and experimentally confirms the heavily saturated growth mechanism demonstrated in Fig. S6.

Material composition of the TiO$_2$ nanostructures

The material properties of the nanostructures that are created in this process have been characterised through energy-dispersive X-ray spectroscopy (EDX), and Raman spectroscopy. The XPS measurements clearly show the introduction of oxygen following the process, while it is practically absent in parts of the Ti samples without nanostructures (Figure S7a). The Raman spectra (Figure S7b) of Ti samples over the range 150-750 cm^{-1} show that areas where nanostructures have been formed have three distinct peaks at 241, 439 and 613 cm^{-1}. These three peaks can be identified as arising from multi-photon process, E_g and A_{1g} active Raman modes for the tetragonal rutile structure of TiO$_2$, respectively. Raman spectra from unexposed sections of the surface have suppressed peaks. Thus, we conclude that the nanostructures comprise predominantly of TiO$_2$ of rutile form. The peaks associated with Al and V arise because the nanostructures under investigation was created on bulk Ti, which was not pure but contained small amounts of Al and V. We also characterised nanostructures created from thin films of Ti on glass substrates. The main results were unchanged, but there were additional peaks associated with the elements found in the glass substrate.
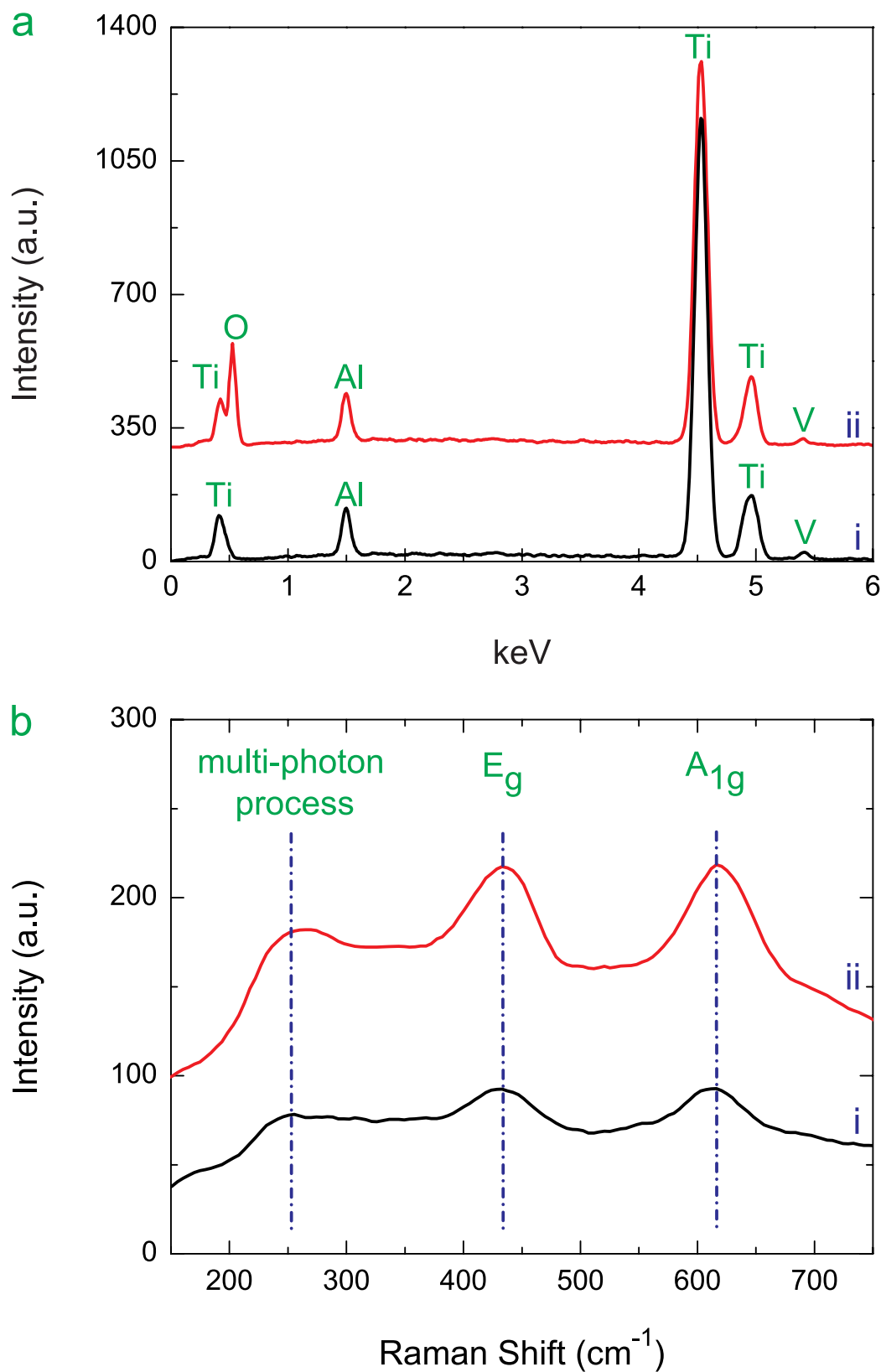
Figure S7. (a) Energy-dispersive X-ray spectroscopy (EDX) obtained from regions of a Ti disk (i)

without and (ii) with the nanostructures. **(b)** Raman spectroscopy obtained from regions of the Ti

disk (i) without and (ii) with the nanostructures.

## Insensitivity of the nanostructure features to laser power and exposure time

A crucial aspect of the formation mechanism reported here is that the nonlinear dynamics of the process, together with the material properties sets the key features such as the nanoline width and nanoline period (Figure S8). The orientation of the structures is determined by the polarisation of the incident pulses. We characterised the dependence of these parameters to exposure time (i.e., the total number of incident pulses) and incident laser intensity. Figure S8 shows the dependence of nanoline width and period on the scan rate and the pulse energy. For these experiments, the pulse duration was ~170 fs, (full-width at half maximum intensity) spot size was 12 μm and repetition rate was 1 MHz. The pulse energy and peak intensity are proportional to incident average power for given pulse duration, repetition rate and spot size. Neither of these parameters lead to a measurable change in the nanoline width or period despite a factor of 4-fold change in the exposure time and a factor of 3-fold increase in pulse energy. This insensitivity to exposure time and pulse power is central to the uniformity of the structures and pave the way to processing of non-planar surfaces. Even if the peak pulse intensity varies due to noise from the laser or displacement of the sample partially out of focus due to a mechanical perturbation or simply because the surface has curvature, the structures are unaffected. In fact, this should allow the creation of the nanostructures not only on non-planar surfaces, but also on rough surfaces. This flexibility is in contrast to conventional laser lithography, which requires the samples to be extremely flat.

With increasing exposure time (reduction of the scanning speed) or pulse energy, the lateral extent over which the nanostructures reach, in other words, the pattern width is increased (Figure S9). This is expected from our theoretical model: As each portion of a nanostructure is created through the nonlinear feedback mechanism, involving scattering from the existing structures, surface points at the edge of the beam, where the total intensity barely exceeds the ablation threshold still grow, but with much smaller growth rates.

18
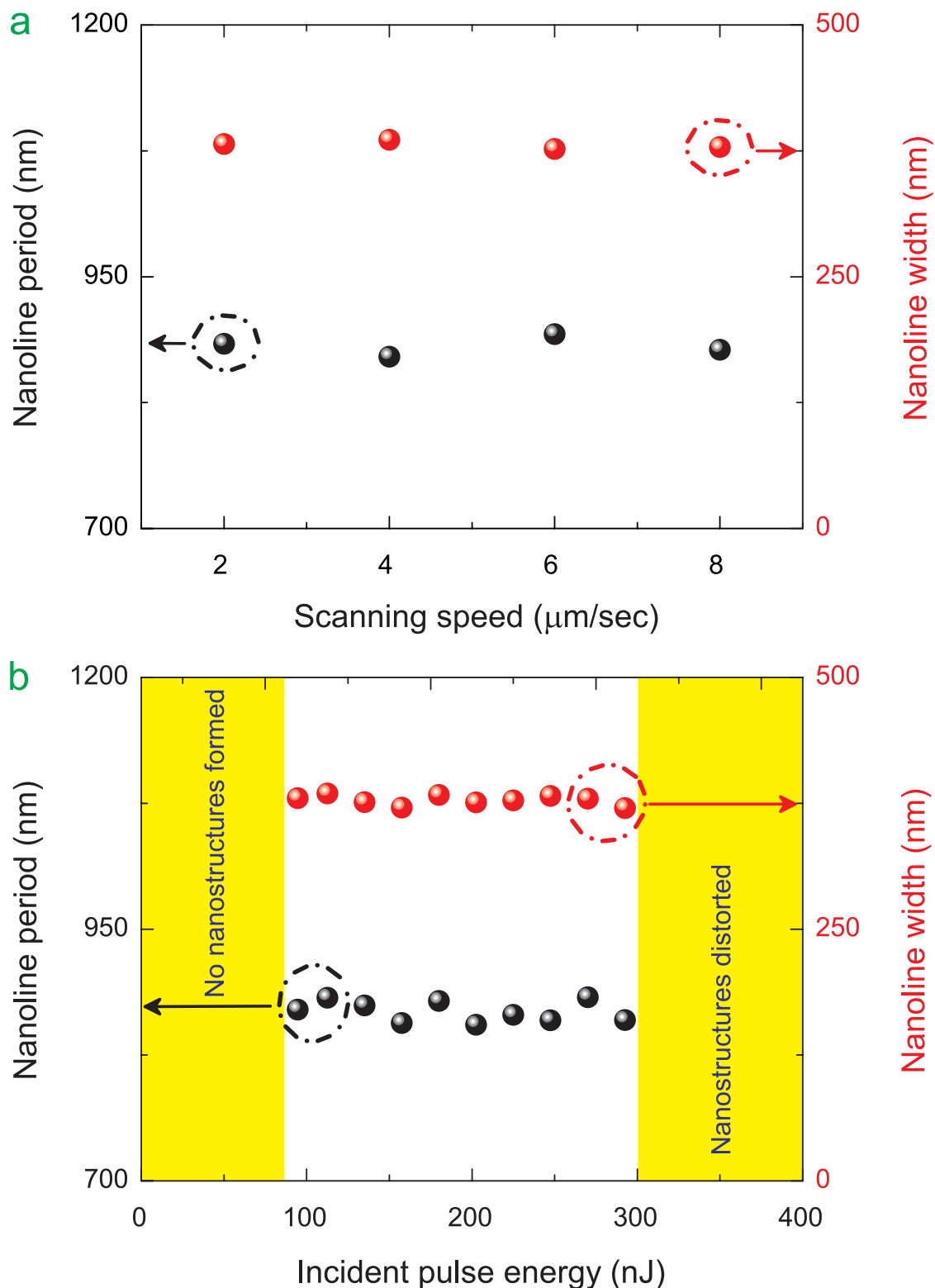
Figure S8. (a) Nanoline width (red circles) and period (black circles) as a function of scanning speed, which controls the exposure time. **(b)** Nanoline width (red circles) and period (black circles) as a function of pulse energy under fixed repetition rate and pulse duration. It is seen that neither exposure time (total fluence), nor peak power affect the width and period.
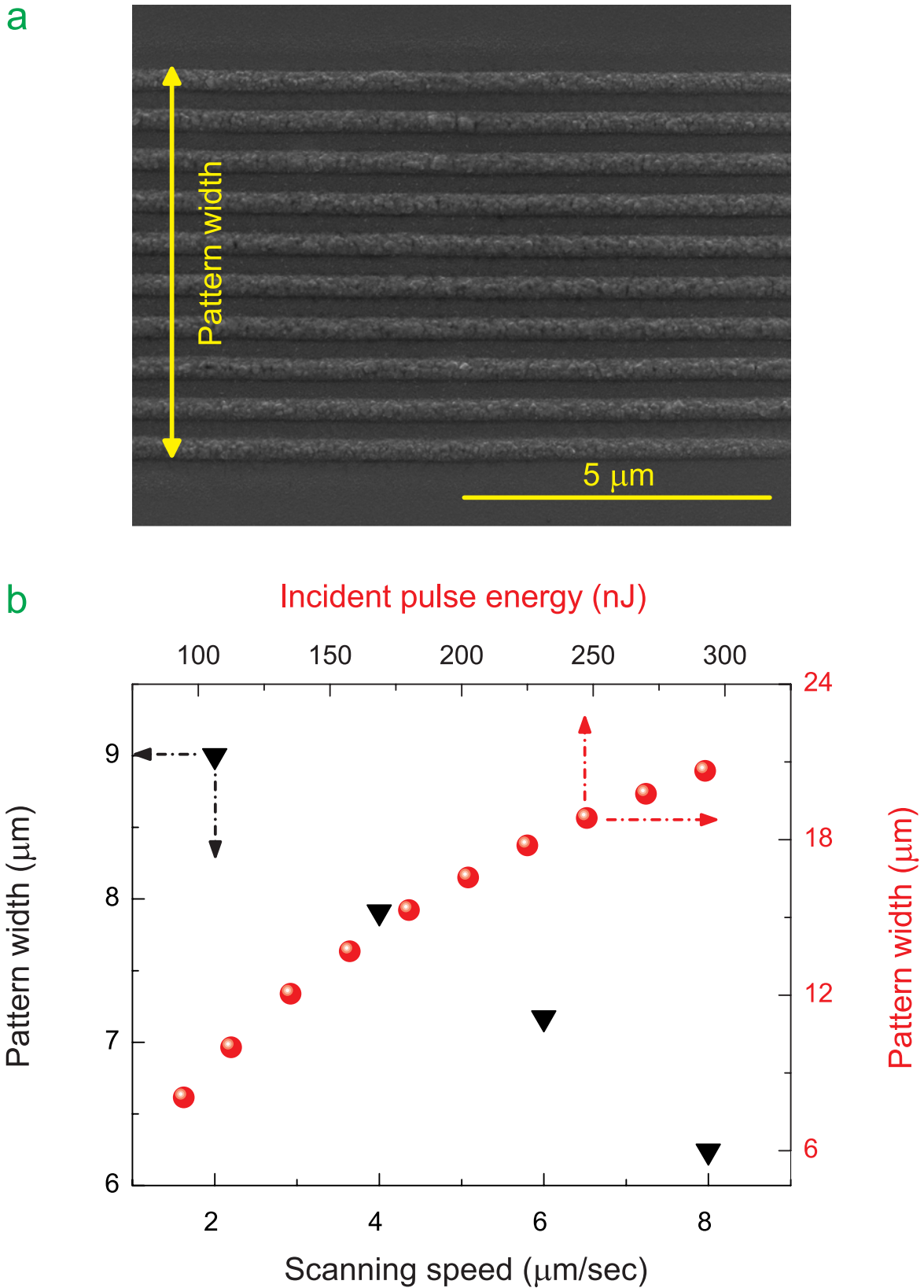
Figure S9. (a) SEM image, where the nanoline pattern width is indicated. **(b)** The width of the pattern of nanolines formed is characterized with respect to scanning speed (to which the exposure time is inversely proportional) (black triangles) and incident pulse energy (red circles).

Characterization of the uniformity of the nanostructures

Given that the nanoline periodicity, as well as the other features of the nanostructures is determined by the nonlinear laser-material interaction, it is important to characterise the long-range uniformity of these structures. We have used atomic force microscopy (AFM) imaging to obtain the surface profile in a thin and long strip perpendicular to the nanolines from the sample shown in Fig. 4b. From this, we have extracted distances between successive peaks (for a total of 69 measured nanoline periods), constituting the nanoline periods of the structure (Fig. S10a). The average value of the nanoline period is 646.18 nm in this experiment. In addition to calculating the standard deviation of these measurements, which yields 0.9 nm, we utilised Allan deviation statistics, a commonly used technique in metrology, to characterise the variation of the nanoline period as we scan over increasingly large distances over the same sample. The modified Allan deviation reaches as low as 0.1 nm. If overlapping Allan deviation is used, similar results are obtained (Fig. S10b). These results are limited by the manufacturer-specified accuracy of the AFM equipment, which is set by temperature-related nonlinearities of the piezo-stages inside it. We believe that the actual uniformity of the period of the structures is likely to be superior since it is determined by lesser stable one of two factors, either the stability of the laser wavelength or the material uniformity of the Ti thin film. The wavelength of the laser used in this study has a measured stability of better than 10^{-7} fractional variation even without any active stabilisation and the thickness of the thin film can, in principle, be controlled at the atomic-layer level. Therefore, it appears plausible that the long-range uniformity of the periodicity is significantly better than the AFM-limited values reported here.
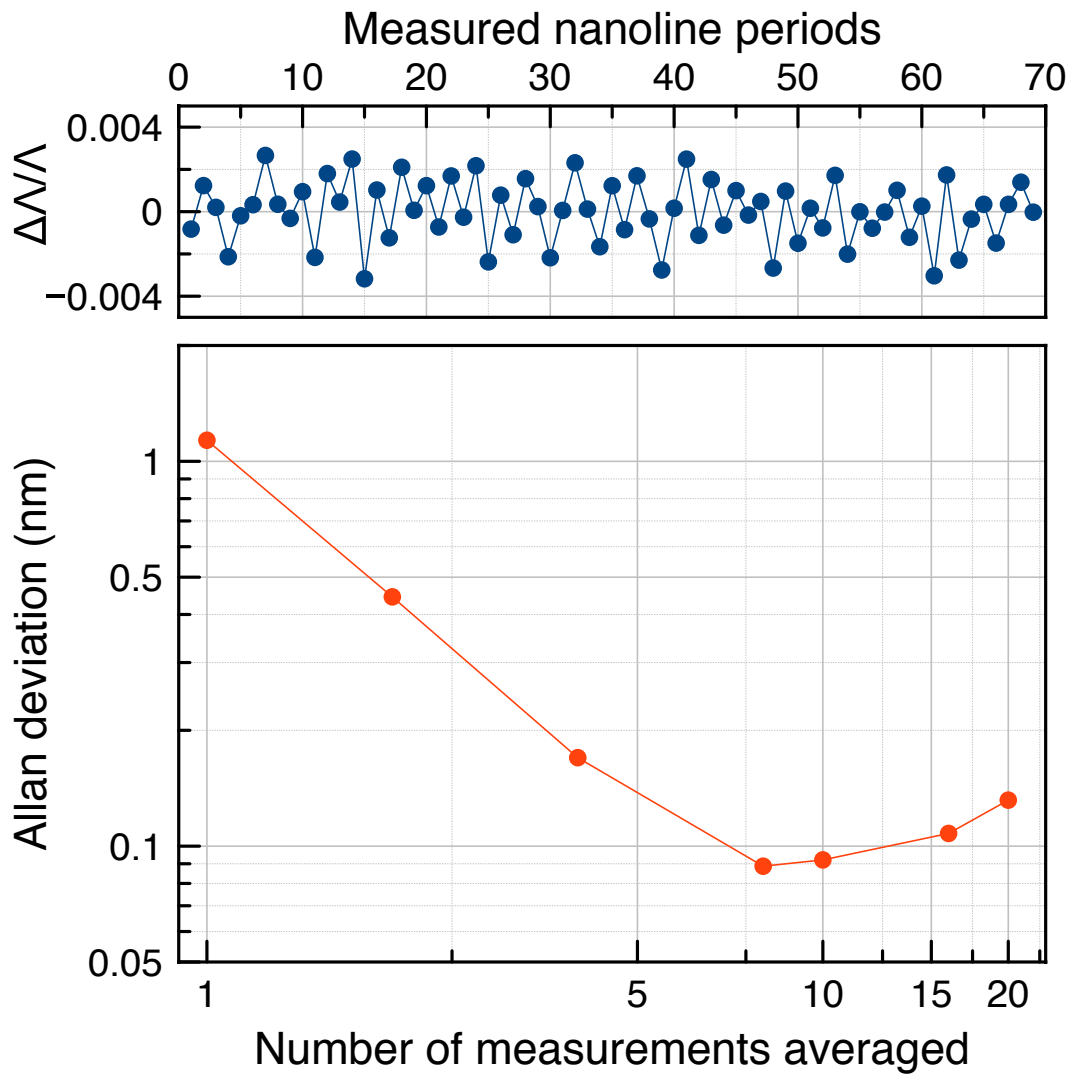
Figure S10. Experimental characterisation of the long-range uniformity. **Upper panel:** Fractional variation of the nanoline period, Λ, for 69 consecutive samples. **Lower panel:** Allan deviation of the nanoline periods for the corresponding data.

Influence of film thickness and laser wavelength

The direction of the nanostructures is directly controlled through the laser polarisation. Other key features, namely the nanoline width and period can be chosen through the thickness of the Ti thin film. For a glass substrate, the nanoline width and period can be varied at least between 330 nm – 400 nm and 610 nm – 790 nm, respectively, for film thicknesses of 50 nm to 300 nm (Figure S11a). Similarly, the nanoline period can be controlled through the laser wavelength, as demonstrated by measurements at 1050 nm with the fibre laser and a regeneratively amplified Ti:sapphire laser system (100 fs-long pulses at 1 kHz repetition rate) (Figure S11b). A fuller characterisation would require a tuneable source of femtosecond pulses, which we did not have access to. However, on-the-fly control over the periodicity and the creation of complex structures should be possible with a tuneable laser source such as an optical parametric oscillator or amplifier.
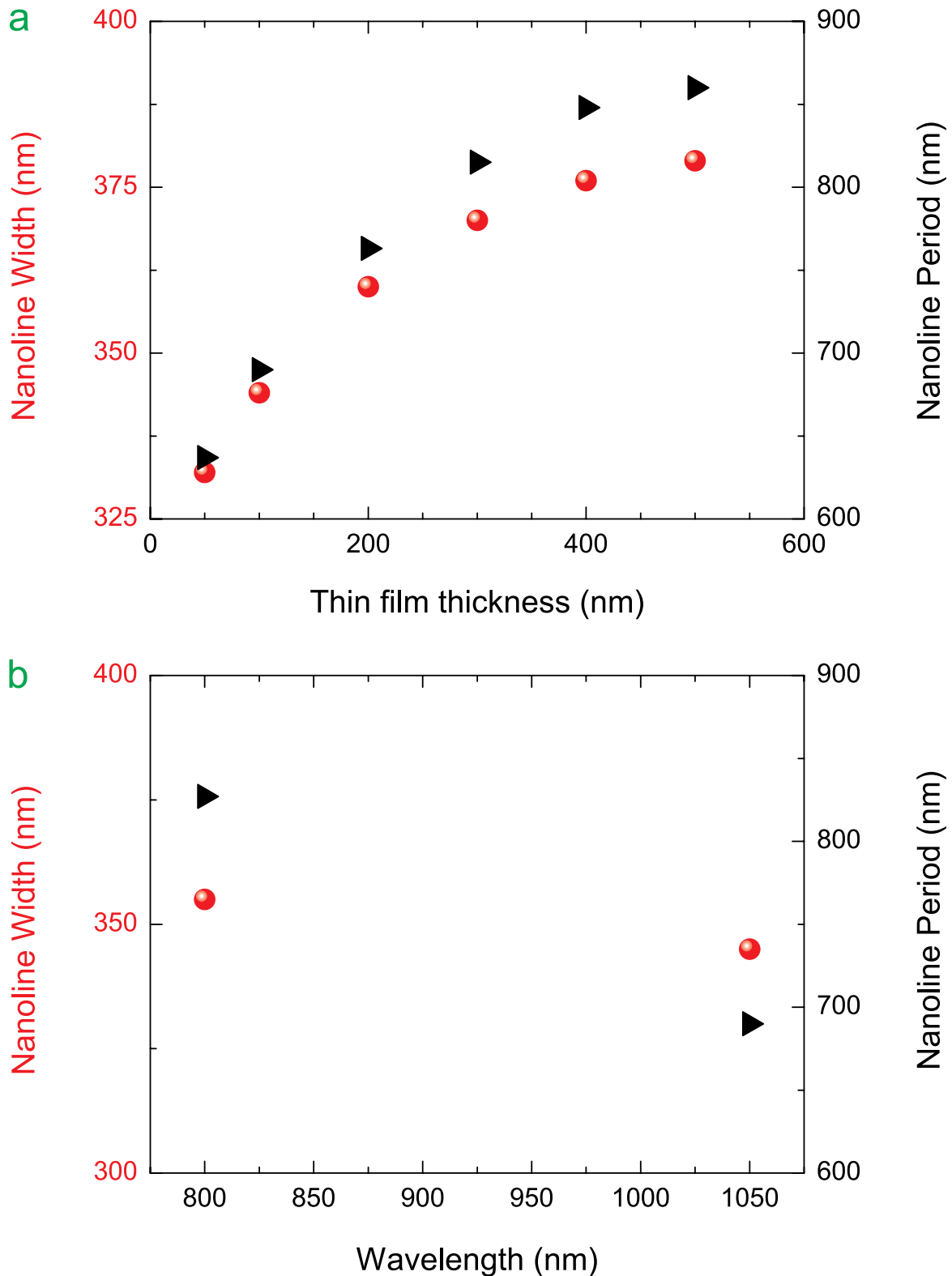
Figure S11. **(a)** Experimentally determined variation of the nanoline width (red circles) and nanoline period (black triangles) as a function of the thin film thickness on glass substrate. **(b)** Experimentally determined variation of the nanoline width (red circles) and nanoline period (black triangles) as a function of the laser wavelength on glass substrate.

24

Analogy to mode-locking dynamics and parabolic profiles of the nanostructures

An analogy can be made between these dynamics and mode-locking of lasers. Mode-locking[6] is similarly initiated from noise, more precisely, from cavity modes with no mutual coherence, by positive feedback due to nonlinear gain and stabilised by negative feedback of the pulse shaping dynamics[7], often in the form of solitons or similaritons[8]. Here, the spatial modes of the surface structure develop coherence as a result of positive feedback, stabilised and made uniform by negative feedback.

Cross-sectional profiles of the nanostructures, measured with AFM and confirmed by scanning electron microscope (SEM) images, are parabolic in shape for all sizes. We note that the nearly parabolic curves used to fit the measured profiles are of the same mathematical form as used to fit temporal shape of the similariton pulses in [9] (Fig. S12), even though the physical systems are entirely different.
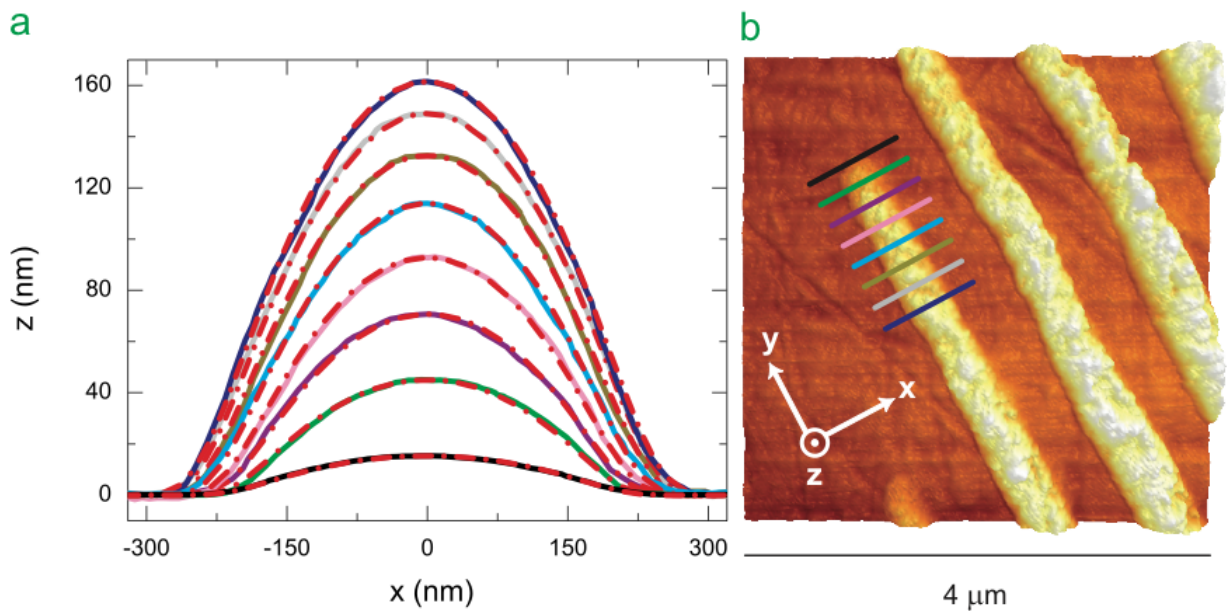
Figure S12. **(a)** Measured cross-sectional profiles (dashed lines) of the nanostructures demonstrating parabolic shape that scales up self-similarly. Solid lines denote parabolic fits. **(b)** AFM image showing the position of the cross-sectional profiles.

Scaling of the nanoline width with the nanoline height

It is informative to consider how the height and width parameters are related. The nanoline height and widths determined from AFM profiles are plotted in Figure S13. It is seen that the height of the nanostructures saturates as the Ti below is depleted and/or the growth process suffocates due to TiO_2 that forms on top effectively blocking the reach of oxygen to Ti below.
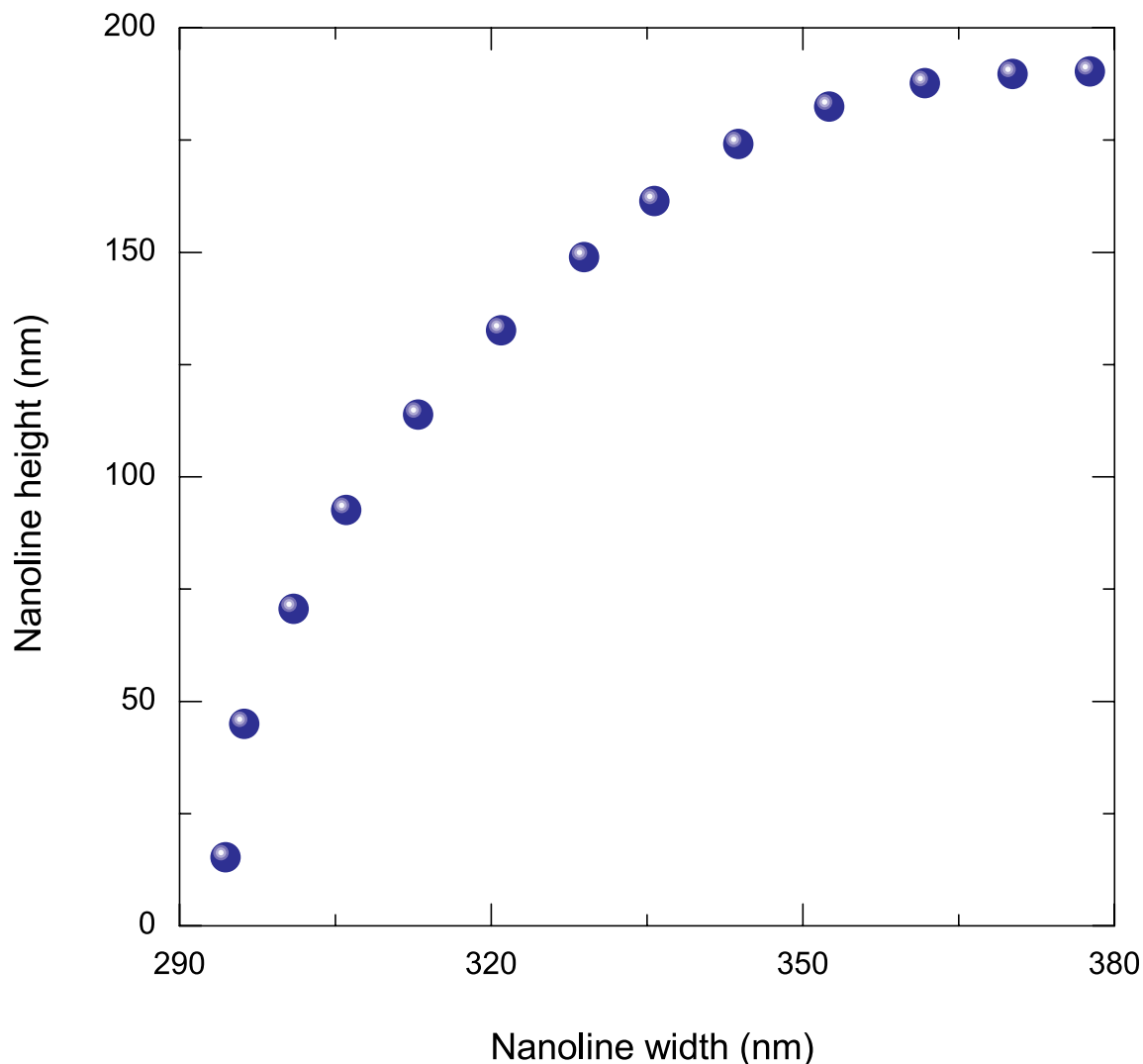
Figure S13. Experimentally determined variation of the nanoline height versus width. Throughout this range, the spatial profile remains parabolic. The sample comprised of a glass substrate covered by a 100 nm-thick Ti thin film.

Thin film preparation

The thin films were deposited by DC magnetron sputtering onto cleaned glass substrates at room temperature. For Ti thin films, we used a Ti target (50.8 mm diameter x 3.17 mm thick, 99.995% pure), mechanically clamped to the DC magnetron cathode of a conventional sputtering system (Vaksis, NanoD-4S). The substrates were cleaned by rinsing in ultrasonic baths of acetone and methanol and dried under nitrogen gas. The base pressure of $2\text{x}10^{-6}$ Torr was obtained in our deposition system and the sputtering was carried out in a 99% pure argon atmosphere. The target-substrate distance was kept at 100 mm during deposition. The ambient argon gas pressure was kept at 8 mTorr for all depositions. The films were deposited at fixed sputtering power of 125 W. The thicknesses of the films used in this study ranged from 50 to 400 nm as confirmed by using optical interferometry and verified by cross-sectional viewing of the thin films by SEM.

References

[1] Hu, W., Shin, Y. C. & King, G. B. Micromachining of Metals, Alloys, and Ceramics by Picosecond Laser Ablation. J. Manuf. Sci. Eng. 132, 011009 (2010).

[2] Gamaly, E. et al. Ablation of metals with picosecond laser pulses: Evidence of long-lived nonequilibrium conditions at the surface. Phys. Rev. B 71, 174405 (2005).

[3] Kara, V. & Kizil, H. Titanium micromachining by femtosecond laser. Optics and Lasers in Engineering 50, 140–147 (2012).

[4] Mannion, P., Magee, J., Coyne, E. & O'Connor, G. M. Ablation thresholds in ultrafast laser micromachining of common metals in air. SPIE Proceedings 4876, 470–478 (2003).

[5] Agrawal, G. P. Nonlinear fiber optics. (Academic Press: 2012).

[6] Haus, H. A. Theory of mode locking with a fast saturable absorber. *J. Appl. Phys.* **46**, 3049–3058 (1975).

[7] Öktem, B., Ülgüdür, C. & Ilday, F. Ö. Soliton-similariton fibre laser. *Nature Photonics* 1–5 (2010).doi:10.1038/nphoton.2010.33

[8] Fermann, M., Kruglov, V., Thomsen, B., Dudley, J. & Harvey, J. Self-similar propagation and amplification of parabolic pulses in optical fibers. *Phys. Rev. Lett.* **84**, 6010–6013 (2000).

[9] Ilday, F., Buckley, J., Clark, W. & Wise, F. Self-similar evolution of parabolic pulses in a laser. *Phys. Rev. Lett.* **92**, 213902 (2004).